# Anisotropic resonant tunneling in twist-stacked van der Waals heterostructure

*Dan Guo[1], Huiwen Wang[1], Liu Yang[1], Weikang Dong[1], Boyu Xu[1], Shuang Du[1], Xuyan Rui[1], Qingrong Liang[1], Kenji Watanabe[2], Takashi Taniguchi[2], Zhiwei Wang[1,]*, Yan Xiong[3,]*, Wei Jiang[1,]*, Jiadong Zhou[1], Shoujun Zheng[1,]**

*[1]Centre for Quantum Physics, Key Laboratory of Advanced Optoelectronic Quantum Architecture and Measurement (MOE), School of Physics, Beijing Institute of Technology, Beijing, 100081, China*
*[2]National Institute for Materials Science, 1-1 Namiki, Tsukuba 303-0044, Japan*
*[3]Analysis&Testing center, Beijing Institute of Technology, Beijing, 100081, China*
*Corresponding email: zhiweiwang@bit.edu.cn, xiongyan@bit.edu.cn, wjiang@bit.edu.cn, szheng@bit.edu.cn*

**ABSTRACT**: Resonant tunneling, with energy and momentum conservation, has been extensively studied in two-dimensional van der Waals heterostructures and has potential applications in band structure probing, multi-valued logic, and oscillators. Lattice alignment is crucial in resonant tunneling transistors (RTTs) for achieving the negative differential resistance (NDR) with a high peak-to-valley ratio (PVR) because twist angle-induced momentum mismatch can break the resonant tunneling condition. Here, we report anisotropic resonant tunneling in twist-stacked $ReSe_2$/*h*-BN/$ReSe_2$ RTTs, where the PVR exhibits a strong dependence on the twist angle between the two $ReSe_2$ layers, reaching a maximum at the twist angle of 102°. Theoretical calculations suggest that the twist angle modulates the joint density of states of the two anisotropic bands in $ReSe_2$ layers during the tunneling process, significantly suppressing the valley current and thereby enhancing the PVR. Double NDR peaks were observed in twist-stacked RTTs, which are attributed to the interband resonant tunneling. Moreover, our twist-stacked RTTs are utilized in multi-bit inverters and adjustable self-powered photodetectors, shedding light on the design of high-performance RTTs and photodetectors *via* twist-stacked engineering.

Keywords: two-dimensional material, anisotropic band, resonant tunneling transistor, van der Waals heterostructure, negative differential resistance, peak-to-valley ratio

## INTRODUCTION

Resonant tunneling (RT), which involves particle tunneling through a barrier with energy and momentum conservation, exhibits a negative differential resistance (NDR), which can be applied in steep-slope switches, oscillators, high-frequency amplifiers, multi-valued logic (MVL), and low-power devices.[1-6] Traditional three-dimensional (3D) RT devices with double-barrier quantum well structure face challenges such as lattice mismatch, impurities, and complex sub-bands,[7,8] which constrain the peak-to-valley ratio (PVR). In contrast, two-dimensional (2D) RT devices present several advantages for fabricating ideal device structures, such as atomically flat transport channels, clean interfaces without covalent bonds, and the feasibility of material selections, ensuring superior performances in RT devices.[9-12] Consequently, the PVR of 2D resonant tunneling transistors (RTTs) was theoretically predicted to be several orders of magnitude higher than that of 3D RT devices.[13] However, the PVR in reported 2D RTTs[14,15] remains relatively low due to high valley current induced by band tail states, with a maximum of ~9 observed in twisted black phosphorus (BP) homostructure *via* the quantum well tunneling mechanism.[16] Therefore, further efforts are required to improve PVR by facilitating device quality and exploring novel RT mechanisms.[17]

Lattice orientation plays a critical role in determining the intrinsic properties and performances of 2D twistronic devices. Modulating the twist angle through stacking engineering in 2D van der Waals (vdW) heterostructures has led to significant advancements in superconductivity, ferromagnetism, and ferroelectricity.[18-20] However, the large twist angle is typically avoided in RTTs because they can introduce momentum mismatch, necessitating compensation through phonons, photons, or plasmons.[21-26] For example, precise alignment of lattice orientations between the top and bottom layers is required to achieve NDR in $MoS_2$-based RTT.[27] A small twist angle is typically introduced in graphene/*h*-BN/graphene devices to observe the NDR peak at a certain voltage.[28,29] Although NDR has been investigated in twisted BP, the PVR in this device is independent on the twist angle.[16] Actually, the twist angle provides an additional degree of freedom to precisely control interlayer coupling and band alignment, which has not been thoroughly explored in RTTs.

RT in 2D RTTs provides a valuable means to probe the intrinsic properties of 2D materials and develop advanced applications as band alignments and carrier densities of 2D materials can be easily modulated by electric field and light illumination.[30-33] For instance, quantum states and chirality of graphene can be explored by manipulating lattice orientations in RTTs.[34,35] Furthermore, multiple NDR peaks caused by RT can be leveraged for information storage with multiple logic states,[36,37] highlighting the potential of RTTs for advanced storage and photodetection applications.

In this study, we fabricated twist-stacked RTTs (TS-RTTs) based on $ReSe_2$/hexagonal boron nitride (*h*-BN)/$ReSe_2$ vdW heterostructures with various twist angles between the top and bottom $ReSe_2$ layers. Unlike traditional 2D RT devices, our TS-RTTs devices exhibit twist angle-dependent anisotropic resonant tunneling (ART) with a maximum PVR of 3.2 at a twist angle of 102°. Theoretical calculations reveal that the band alignment between anisotropic bands generates twist angle-dependent joint density of states (JDOS), suppressing the valley current and improving the PVR. The NDR behavior is also significantly influenced by temperature and light illumination. Additionally, double NDR peaks were observed in TS-RTTs, which is attributed to RT between multiple anisotropic sub-bands of $ReSe_2$. Furthermore, we developed a ternary inverter for MVL and a tunable self-powered photodetector based on the TS-RTTs.

## RESULTS AND DISCUSSION

### Anisotropic Resonant Tunneling.

Momentum conservation in vdW heterostructure can be effectively manipulated by altering the lattice orientation through the twist angle, providing an additional degree of freedom to modulate RT conditions. In distorted 1T rhenium diselenide (1T'-$ReSe_2$), rhenium atoms form

Re-chains along the *a*-axis, resulting in an in-plane anisotropy (shown in Figure 1a). Theoretical calculations indicate that the conduction bands of 1T'-$ReSe_2$ exhibit significant band anisotropy, consistent with the C2 symmetry of the T' phase $ReSe_2$ (see Figure 1b). The anisotropy shows a 40° angle difference between the first conduction band (CB-1) and the second conduction band (CB-2) at Gamma (Γ) point. This unique anisotropic band structure enables precise tuning of momentum matching and interband tunneling by designing vdW heterostructures with tunable twist angles.

$ReSe_2$ is an n-type semiconductor with electron mobility of ~5.66 $cm^2V^{-1}S^{-1}$ (see Figure S1) where the conduction band minimum is located at the Γ point (shown in Figure 1c). In $ReSe_2$/*h*-BN/$ReSe_2$ vdW heterostructure, electrons near the Γ point can maintain momentum conservation even at a large twist angle of two $ReSe_2$ layers, enabling a RT. Simultaneously, the momentum mismatch significantly reduces the JDOS in other regions of momentum space, leading to a decrease in valley current (as shown in Figure 1d). Therefore, it is theoretically feasible to enhance the PVR in some specific TS-RTTs *via* precise control of the twist angle.

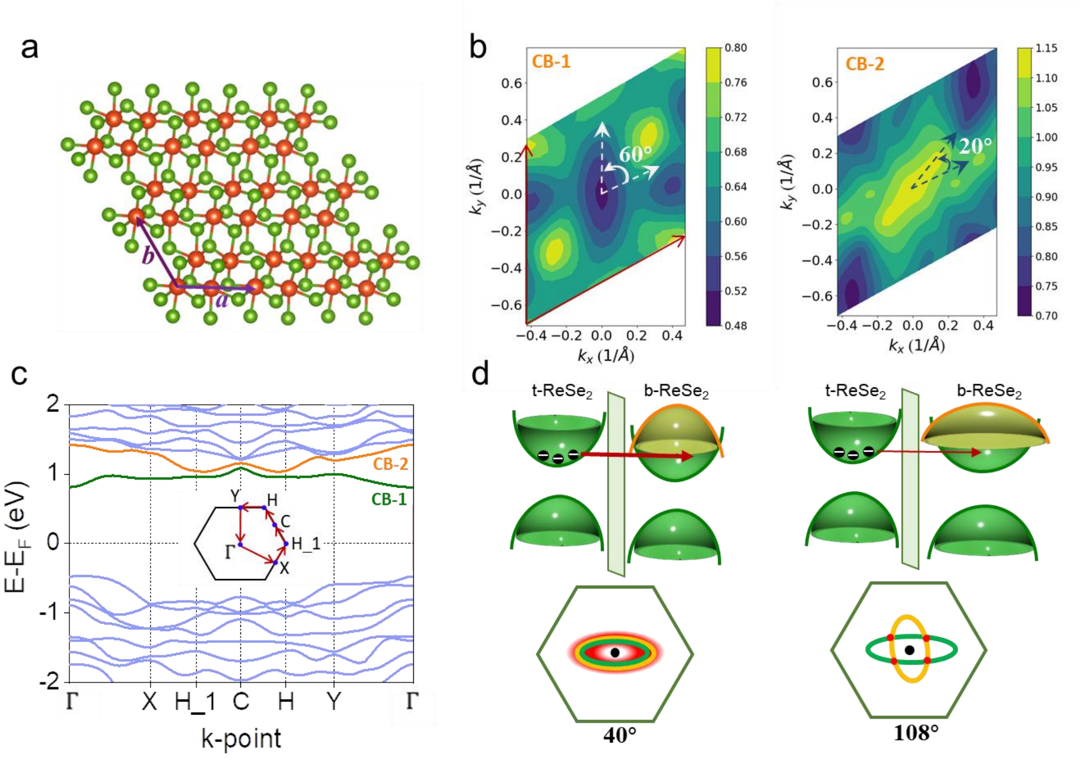


Figure 1. ART based on the anisotropic bands of 1T'-$ReSe_2$. (a) Top view of the atomic structure of 1T'-$ReSe_2$, exhibiting the anisotropic lattice orientations. (b) Calculated band maps of the first conduction band (CB-1, left) and the second conduction band (CB-2, right), clearly demonstrating the strong in-plane anisotropy. (c) Band structures of monolayer $ReSe_2$, showing the conduction band minimum at the Γ point. (d) Schematic band alignments of the $ReSe_2$/*h*-BN/$ReSe_2$ RTTs with 40° (top left) and 108° (top right) twist angles. The JDOS in the 108° TS-RTT (red points in bottom right) is lower than that in the 40° TS-RTT (red shadow in bottom left). ART is expected in the TS-RTT with a specific twist angle by suppressing the valley current.

**Negative differential resistance in a 102° TS-RTT.**

To investigate ART, we prepared a twist-stacked $ReSe_2$/*h*-BN/$ReSe_2$

vdW heterostructure with a twist angle of 102° (device 1). The schematic of TS-RTT is shown in Figure 2a, where a bias voltage is applied to the bottom $ReSe_2$ layer and a back gate voltage is used to tune the carrier densities and Fermi levels of both the top and bottom $ReSe_2$. The TS-RTT is composed of two $ReSe_2$ flakes and a four-layer *h*-BN flake (see the optical image in Figure 2b). The twist angle of the TS-RTT was determined to be 102° by measuring the polarization-dependent Raman spectra of 127 $cm^{-1}$ mode (shown in Figure 2c and Figure S1). Figure 2d shows the cross-section image of transmission electron microscopy (TEM), indicating the twist-stacked order between the top and bottom $ReSe_2$ layers, and the top and bottom $ReSe_2$ layers were identified to consist of approximately 5 layers and 4 layers, respectively. Monolayer and bilayer $ReSe_2$ are not working well in our experiments which may be due to the instability of $ReSe_2$ and interfacial disorders.

Clear NDR peaks are observed in the 102° TS-RTT at various gate voltages of 20 V, 40 V, 60 V, and 80 V at 10 K (shown in Figure 2e). The positions of these NDR peaks shift to smaller bias voltages with increasing gate voltage (as shown in Figure 2g). This trend is further evident in the conductance map as a function of bias and gate voltage, illustrated in Figure 2f. Notably, the PVR improves with increasing gate voltage, as summarized in Figure 2g.

It is noteworthy that the NDR behavior in our TS-RTT exhibits a strong dependence on temperature (shown in Figure 2h), while it is weakly affected by temperature in the previously reported RTTs (Figure 2i).[15,27] Figure 2h shows that NDR peaks progressively weaken and eventually disappear with increasing temperature from 10 K to 300 K at a fixed $V_g$ of 40 V. Moreover, both the tunneling current and NDR are influenced by light illumination with a 520 nm laser, which is displayed in Figure 2j at various laser powers of 0.6 μW, 6.1 μW, and 18.2 μW at 10 K. The sensitivity of NDR peaks to temperature and light illumination suggests that the NDR behavior is associated with the specific band alignment and the twist angle-induced momentum mismatch. The applied bias voltage drives the Fermi level of the conduction band in the top $ReSe_2$ to align with the corresponding conduction band in the bottom $ReSe_2$, producing a RT. As the bias voltage increases, band misalignment and momentum mismatch occur in the TS-RTT, leading to a sharp decrease of the PVR.

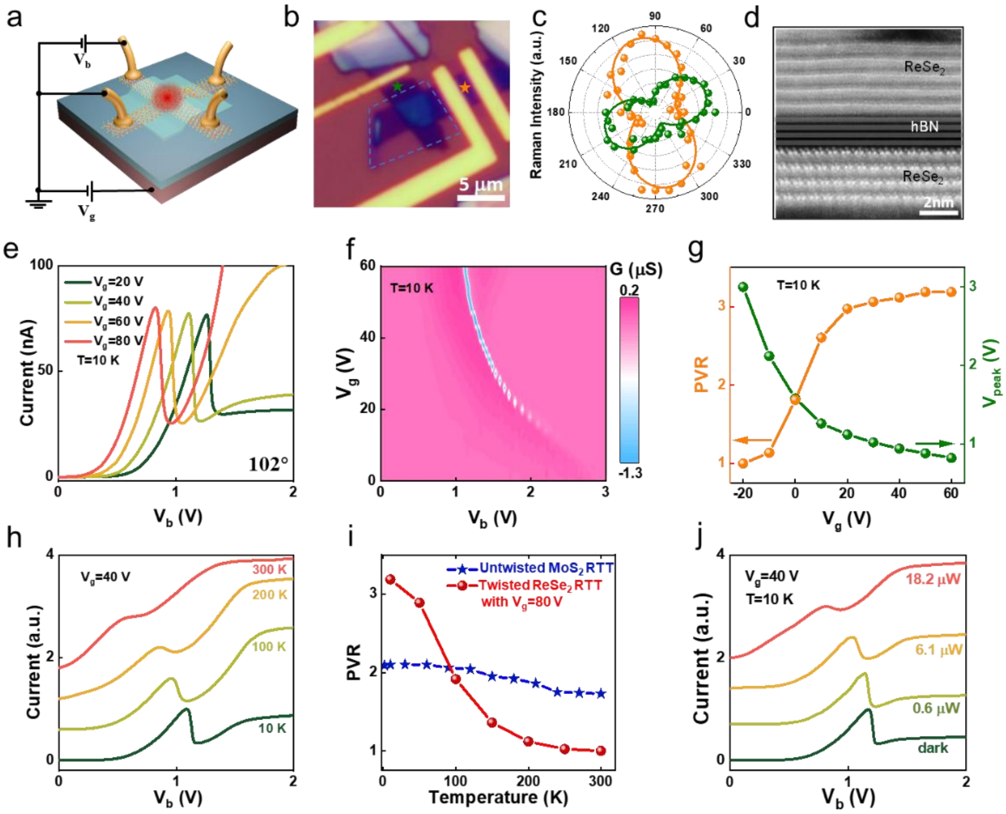

Figure 2. Negative differential resistance in a 102° twist-stacked RTT. (a) Schematic of the $ReSe_2$/*h*-BN/$ReSe_2$ TS-RTT, where a bias voltage is applied to the bottom layer of $ReSe_2$ and RT occurs at the overlapping region (shown in the red region). (b) Optical image of the 102° TS-RTT (device 1), with orange and green pentagons indicating the locations for Raman testing. Two $ReSe_2$ layers are separated by a few-layer *h*-BN (blue dashed line). (c) Polarization-dependent Raman intensity of both top (orange circles) and bottom (green circles) $ReSe_2$ layers at Raman shift of 127 $cm^{-1}$. Fitted lines (orange and green lines) of Raman data show that the twist angle between the two $ReSe_2$ is about 102°. (d) TEM cross-section image of the TS-RTT, showing the relative lattice orientation of two $ReSe_2$. (e) Tunneling current as a function of bias

voltage at different gate voltages with T=10 K, clearly demonstrating the gate-dependent NDR. (f) Conductance map of the 102° TS-RTT with T=10 K, showing a trend of NDR peak with gate voltage. (g) Summary of PVR and NDR peak positions as a function of gate voltage with T=10 K. (h) Tunneling current as a function of bias voltage at various temperatures with $V_g$=40 V, showing that NDR is sensitive to temperature. (i) Comparison of temperature-dependent PVR between the TS-RTT with $V_g$=80 V and an untwisted RTT based on monolayer $MoS_2$. (j) Tunneling current as a function of bias voltage under 520 nm light illumination with various laser powers at $V_g$=40 V and T=10 K.

**Double NDR Peaks in TS-RTT.**

Based on the ART between anisotropic conduction bands in $ReSe_2$, multiple NDR peaks in TS-RTTs are expected. TS-RTTs with various twist angles were fabricated and double NDR peaks were observed (device 2 and device 3). Twist angles of device 2 and device 3 are determined to be 87° (Figure S2) and 37° (Figure S4) by polarization-dependent Raman spectra. In contrast to device 1, both device 2 and device 3 exhibit two gate-dependent NDR peaks (as shown in Figures 3a and 3d) and distinguishable NDR regions (Figures 3b and 3e) at 10 K. Although the NDR peaks weaken with increasing temperature in Figure 3c at a fixed gate voltage of 80 V, it is worth noting that the second NDR peak decays faster than the first, suggesting the different origins between the two peaks (more information of devices 2 and 3 can be found in Figures S3 and S5). Similar to device 1, double NDR peaks and conductance of devices 2 and 3 show a strong dependence on gate voltage, temperature, and light illumination. Capacitance-voltage (*C*-*V*) measurement is also an efficient tool to probe NDR peaks as RT-induced conductance variation affects the capacitance of vdW heterostructure. Even though only two NDR peaks were observed in the *I*-*V* measurement in device 3, three NDR peaks were observed in the *C*-*V* measurement at 10 K (Figure S5g), suggesting that *C*-*V* measurement is a more sensitive tool to identify the conduction band of $ReSe_2$.

The observed double NDR peaks can be attributed to the RT between different conduction bands of $ReSe_2$. There are several conduction bands at the Γ point according to our theoretical calculations (Figure 1c). The second NDR peak arises from the band alignment between CB-1 in the top layer and CB-2 or the higher conduction bands in the bottom layer (shown in Figure 3f). The band dispersion relation determines the RT condition, resulting in the NDR peaks being sensitive to temperature and light illumination. Specifically, the second NDR peak in the RTT with the twist angle of 37˚ is attributed to the 40° anisotropic angular difference between the first and second conduction bands of $ReSe_2$. The double peak observed at twist angle of 87° might originate from RT between the first conduction band at the Γ point of one $ReSe_2$ layer and other conduction bands (like the third conduction band) of the other $ReSe_2$ layer, which needs further investigation.

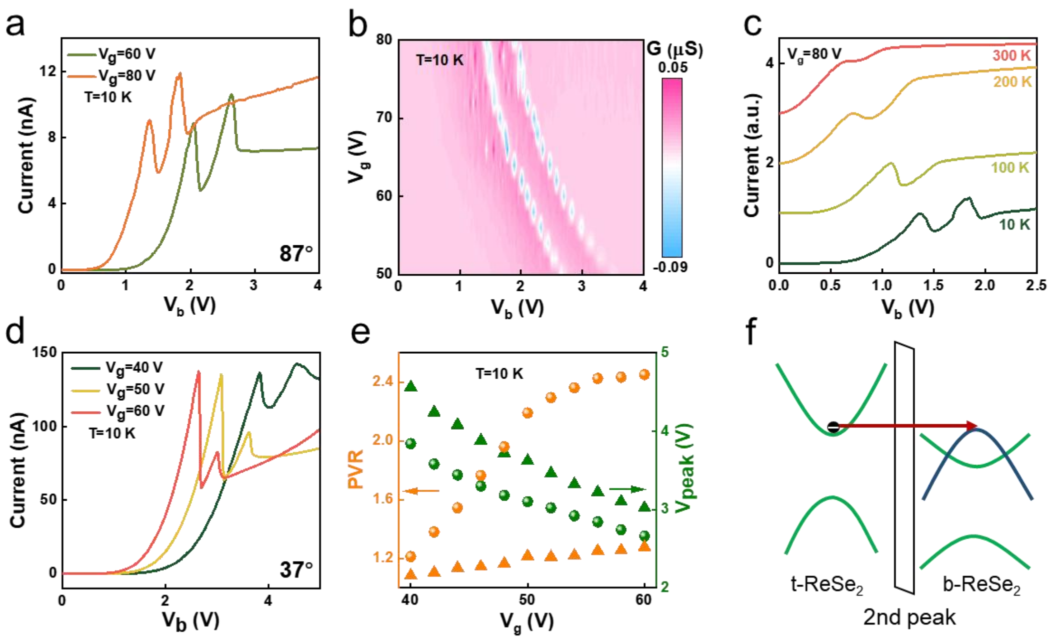


Figure 3. Double NDR peaks in TS-RTTs. (a) Tunneling current as a function of bias voltage at different gate voltages in an 87° TS-RTT with T=10 K, showing double NDR peaks. (b) Conductance map of the 87° TS-RTT with T=10 K, showing NDR peaks change with gate voltage. (c) Tunneling current as a function of bias voltage for the 87° TS-RTT at different temperatures with $V_g$=80 V, exhibiting that the second peak is more sensitive to temperature. (d) Tunneling current as a function of bias voltage at different gate voltages for a 37° TS-RTT with T=10 K, showing similar double NDR peaks. (e) Summary of PVR and NDR peak positions as a function of gate voltage for the 37° TS-RTT with T=10 K. (f) Schematic of the band alignment, explaining the origin of the double

NDR peaks.

**Twist Angle Dependent PVR.**

Interestingly, NDR is also observed at 10 K in TS-RTTs with various twist angles, including 1.8° (Figures S9 and S10), 31° (Figures S12 and S13), 45° (Figures S14 and S15) and 158° (Figures S6-S8) shown in Figures 4a-d. More devices encapsulated with *h*-BN were also fabricated including twist angles of 7.5° (Figure S16 and S17), 10° (Figure S18 and S19), 140° (Figure S20 and S21), and 160° (Figure S22 and S23). The thicknesses of $ReSe_2$ in those devices are around 4~5 layers, which is similar to that of device 1 (see the AFM images in the supporting information). NDR of all devices exhibits a strong dependence on gate voltage, temperature, and light illumination.

We can see that the tunneling current of 1.8° TS-RTT is the largest (Figure 4a), which can be attributed to the largest JDOS with momentum conservation. It is clear that PVR strongly depends on the twist angle and reaches a maximum of 102° by summarizing PVR values of TS-RTTs with different twist angles (shown in Figure 4e). Note that the absolute value of tunneling current decreases by two orders of magnitude when a large twist angle is introduced. However, the valley current decreases faster than the peak current, resulting in an enhancement of PVR.

To simulate the tunneling current through the *h*-BN layer, we calculated the tunneling probability between the top and bottom $ReSe_2$

layers of a 108° device as shown in Figure 4f (see details in methods). The external electric field drives the Fermi level to the second conduction band, leading to the appearance of the second NDR peak, which agrees very well with double NDR peaks observed in the experimental results (Figure 4e). Further, we calculated the tunneling probability by varying the twist angle between the top and bottom $ReSe_2$ layers (shown in Figures S24 and S25), where the valley current is determined by the tunneling probability of all conduction bands between the top and bottom $ReSe_2$ layers. Due to the anisotropy of the $ReSe_2$ structure, the tunneling probability depends not only on the energy matching condition but also the twist angle-induced momentum matching condition. The bands between the top and bottom $ReSe_2$ layers can reach the largest (smallest) momentum mismatch when the anisotropic angle is about perpendicular (parallel) to each other. For example, the PVR reaches a maximum when the valley current reaches its minimum value at the twist angle of 108° as JDOS is lowest (shown in Figure 4g and Figure S26), which qualitatively agrees well with our experimental results.

PVR in our tunneling devices is determined by both the peak and valley currents. Due to the nature of the Γ point (k=0), the momentum of electrons near the Γ point is insensitive to the twist angle so that we can observe RT at the Γ point even with a large twist angle between the two layers of $ReSe_2$ (Figure S27). The high PVR is attributed to the suppression of valley current *via* twist angle-induced momentum mismatch and twist angle-dependent JDOS between the top and bottom layers. In addition, two bands are predicted to be the largest mismatch at the twist angle of 18° which can also result in the smallest valley tunneling probability and a large PVR. However, the PVR in experimental devices around 18° is not greatly improved, which might be attributed to the high valley current produced by the RT from other momentum spaces. The quantitative mismatch between experimental and theoretical results at smaller twisting angles close to 0° might be attributed to interfacial scattering-induced direct tunneling and large leakage current. Moreover, the momentum match in all momentum space in the RTT with a 1.8° twist angle increases the tunneling probability of electrons, resulting in a large valley tunneling current and the mismatch between experimental and theoretical results.

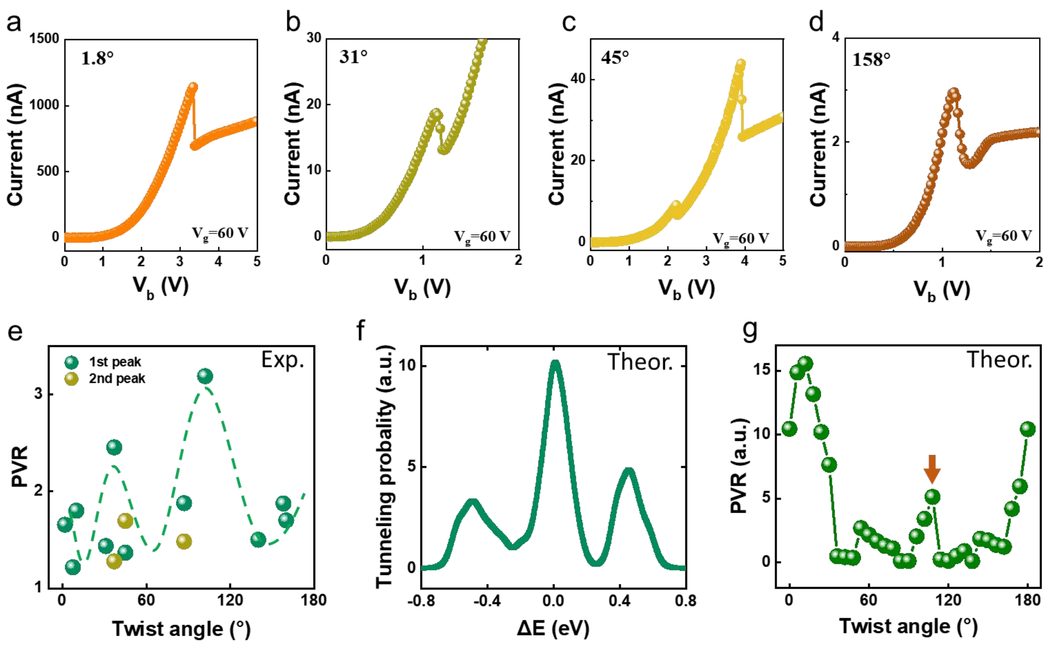

Figure 4. Summary of NDR at various twist angles at 10 K. (a-d) Tunneling currents as a function of bias voltage for TS-RTTs with twist angles about 1.8° (a), 31° (b), 45° (c), and 158° (d), respectively. (e) Summary of PVR as a function of twist angle, showing that PVR is enhanced in the TS-RTT with a large twist angle. The green dashed line is for guidance. (f) Calculated tunneling probability as a function of energy shift for TS-RTT with a twist angle of 108°. (g) Calculated PVR as a function of twist angle, which is consistent with the experimental results in (e).

**Ternary MVL and Photo Response of TS-RTTs.**

MVL has garnered significant attention due to its potential for storing more data in smaller spaces compared to binary logic. In gate-controlled RT devices, negative transconductance can be achieved through NDR. Interestingly, the transfer curve of device 4 (with a twist angle of 158°) exhibits anti-bipolarity at 10 K (as shown in Figures S8a and S8b). Inspired by this, we constructed a ternary inverter with three logic states as depicted in Figure 5a to achieve MVL applications.

The ternary inverter consists of a $ReSe_2$ field-effect transistor (FET) and our TS-RTT (device 4) in series. A bias voltage is applied to the $ReSe_2$ FET which is connected in series with the bottom $ReSe_2$ layer of the TS-RTT, and the top $ReSe_2$ layer is grounded as the source. The input voltage ($V_{in}$) serves as the back gate for device 4, and the output voltage

($V_{out}$) is measured at the shared electrode between $ReSe_2$ FET and device 4. The input-output characteristic ($V_{out}$ versus $V_{in}$) of the inverter is shown in Figure 5b. As $V_{in}$ varies from 0 V to 60 V, $V_{out}$ exhibits three distinct states: (i) $V_{out}$ is 5 V when 0 V < $V_{in}$ < 10 V (State "2"), (ii) $V_{out}$ is 4.5 V when 20 V < $V_{in}$ < 35 V (State "1"), and (iii) $V_{out}$ is 0 V when 55 V < $V_{in}$ < 60 V (State "0"). The inset in Figure 5b depicts the input-output voltage equivalent table for our ternary inverter. Figure 5c plots the corresponding gains of the inverter at different bias voltages. Two peaks are clearly observed, corresponding to the voltage gains from logic "2" to "1" and "1" to "0". Notably, the gain of the TS-RTT increases with bias voltage, indicating its potential applications in storage and computing. However, due to the low output voltage, our inverter is not scalable. To drive the next logic gate, the output voltage of the inverter must be amplified. Therefore, improving the output voltage of the inverter will be our focus in the future.

Since light illumination significantly affects the negative resistance peak position and PVR, our TS-RTTs are also promising in photodetection applications. We conducted a detector of photo response and photovoltaic response of device 5 (1.8°) at room temperature. The photocurrent increases with increasing the laser power at an applied gate voltage of -40 V, with an on/off ratio of ~$10^6$ and responsivity of 1.2 mA/W at P = 13.8 μW (shown in Figure 5d and Figure S11). It is worth noting that our device shows a responsivity that gradually increases with increasing laser power, which is different from typical photodetectors. We believe this is due to the presence of the *h*-BN barrier in our tunneling device, which makes it difficult for photoelectrons to be collected at low optical power. Only when the optical power increases to a level where enough photoelectrons are generated can they overcome the barrier and be collected by the device's source-drain electrodes. Furthermore, the increased optical power may also lead to a more significant photothermal effect, which could be another reason for the higher responsivity. Additionally, we found that the device has a tunable photovoltaic effect which can be adjusted by changing gate voltage as shown in Figure 5e. The adjustable photovoltaic current can also be confirmed by endurance measurement under periodic illumination at $V_g = \pm 40$ V (shown in Figure 5f), showing its potential applications in self-powered optoelectronic devices, real-time imaging and artificial synapses, *etc*.

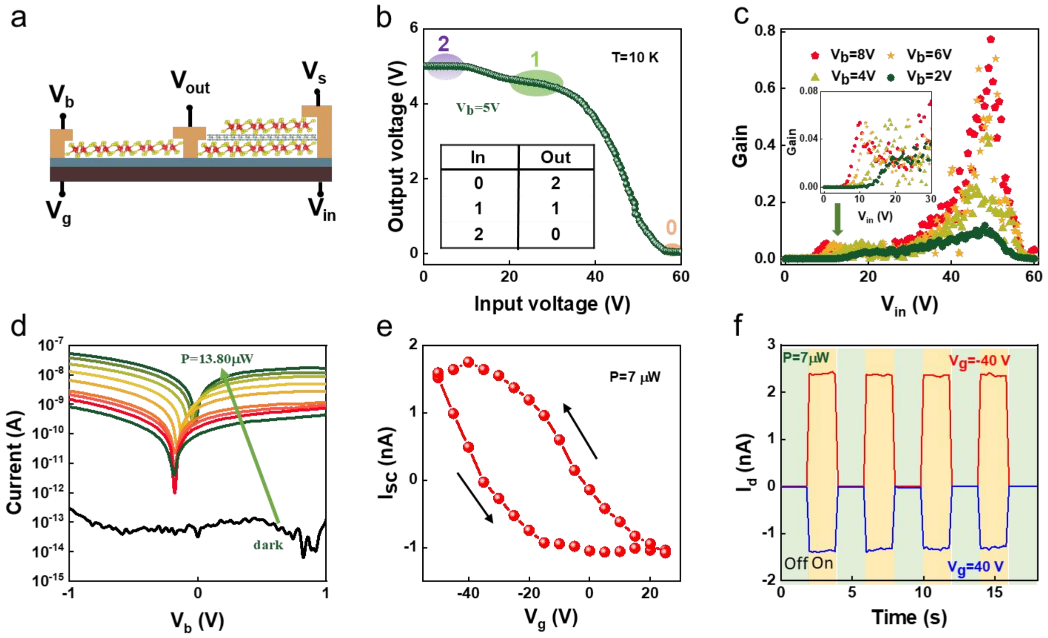

Figure 5. MVL inverter and adjustable self-powered photodetector applications of TS-RTTs. (a) Schematic of a ternary inverter composed of a 158° TS-RTT and a $ReSe_2$ FET. (b) Output voltage as a function of input voltage for the inverter at 10 K, demonstrating the recognition of ternary values. (c) Gain as a function of input voltage. (d) Power-dependent photocurrent as a function of bias voltage for a 1.8° TS-RTT. (e) Gate-dependent photovoltaic current, showing the tunability of the self-powered photodetector. (f) Endurance measurement of photovoltaic current at ±40 V gate voltages.

## CONCLUSIONS

In summary, we reported the ART in $ReSe_2$/*h*-BN/$ReSe_2$ TS-RTTs with various twist angles between the two $ReSe_2$ layers in terms of the in-plane anisotropy of $ReSe_2$. Due to the band anisotropy of $ReSe_2$, our devices exhibited distinct NDR peaks and improved PVR by modulating the twist angle. This enhancement of PVR is attributed to the suppression of valley current within the tunneling process with a specific twist angle of 102°, achieved through unique band alignments and JDOS decrease, as corroborated by our theoretical calculations. Furthermore, we demonstrated that our TS-RTTs have potential applications in MVL inverters with three logic states and in adjustable self-powered photodetectors. Our findings not only introduce a twist-stacking technique to improve the performance of RTTs through twist angle and momentum matching, but also demonstrate its potential applications in programmable optoelectronics and neuromorphic devices.

## METHODS

**TS-RTTs Fabrication.** $ReSe_2$/*h*-BN/$ReSe_2$ twist-stacked heterojunctions were prepared using a dry transfer technique. The bottom $ReSe_2$ was mechanically exfoliated using 3M scotch tape on flake blocks onto a silicon/silicon dioxide (285 nm) (Si/$SiO_2$) substrate for optical microscopy examination (Olympus). Subsequently, *h*-BN was mechanically exfoliated and transferred onto the bottom $ReSe_2$ to serve as the barrier layer. Poly (Bisphenol A carbonate) (PC) film coated on polydimethylsiloxane (PDMS) was used to pick up *h*-BN flakes and release them at 180°C. The PC was prepared by dispersing 1 g of polycaprolactone in 10 mL of chloroform (Aladdin Tech. Co.). The PC was then removed by soaking in chloroform for 5 minutes. Finally, the top $ReSe_2$ was mechanically exfoliated and transferred onto the *h*-BN layer. The entire device was fabricated through a step-by-step transfer method from bottom to top and the edge of the top $ReSe_2$ layer is rotated with respect to the edge of the bottom $ReSe_2$ layer to ensure a twist angle between two layers. Use electron-beam lithography technology (Zeiss supra 55 and Raith ELPHY Quantum) to pattern the electrons of the device, and deposit Cr/Au (5 nm/50 nm) with thermal evaporation in a high vacuum of $10^{-5}$ Pa by a thermal evaporation coater (Chinese Academy of Sciences Shenyang Scientific Instruments Co.).

**Optical Measurement.** The thickness of materials was performed using atomic force microscopy (Dimension Icon, Bruker). Raman and the polarization-dependent Raman spectra measurements were characterized using confocal Raman microscopy (WITec). The TEM image was obtained by an FEI Themis Z with double aberration correctors, and the data was processed by the Velox software.

**Photoelectronic Measurement.** Photoelectric measurements were performed in a probe (CRX-6.5K, Lakeshore) using a semiconductor analyzer (Keysight B1500A). 520nm laser (NBeT) was introduced directly into the probe shore cavity through an optical fiber and the light intensity was measured by a power meter (THORLABS GmbH).

**DFT Calculation Details.** The calculations of electronic properties were carried out based on the density functional theory (DFT). We used the PAW pseudo potential[38] and PBE exchange-correlation functional,[39] as implemented in the Vienna ab initio simulation package (VASP).[40] To avoid the interaction between slabs, we introduced a vacuum layer larger than 15 Å along the z direction. Considering vdW interactions between $ReSe_2$ layers, we applied the DFT-D3 functional when calculating multilayer $ReSe_2$ systems. To obtain accurate electronic band structures where free carriers are located, we chose 0.4 × 0.4 reciprocal patch with respect to reciprocal vectors centered around the Γ point with a 7 × 7 × 1 k-mesh. The lattice parameters were chosen as a=6.64 Å, b=6.77 Å, c=38.96 Å, α=90.0°, β=90.0°, and γ=118.9°.

Tunneling current simulations: To simulate the tunneling current between the top and bottom $ReSe_2$ layers through the middle insulating *h*-BN layers. We calculated the tunneling probability between the electronic states of these two $ReSe_2$ layers under different electric fields and rotational angles. For simplicity, we consider only the conduction band and tunneling between the same wave vectors. Given that the free carriers are mainly located at the bottom of the conduction band, which is centered around the ~~Gamma (Γ)~~ point, we focused on a small 0.4 × 0.4 k patch. We shifted the chemical potential of the top layer electronic states to simulate the gating field. Furthermore, under the large gating field, we assumed that when the energy of electronic field equals the energy difference between the two conduction bands, electrons will tunnel from the first conduction band to the second conduction band. As the top and bottom layers are widely separated by the large-gap insulating layer, the lattice rotation-induced interlayer coupling is neglected, which results in only the rotation of the k-space electronic band structure. To obtain the direct tunneling probability, we calculate the energy difference between the top and bottom layer electronic states (first and second conduction bands) with the same k points. The tunneling probability reads

$$f(\Delta E) = \frac{1}{e^{(E_T^i - E_B^i - \Delta E)/k_B T} + 1}$$

where we take T=300 K, $k_B$ is the Boltzmann constant, ΔE is the electric field strength, and $E_T^i$, $E_B^i$ denote the energy of different bands for the top and bottom $ReSe_2$ layers, respectively. For example, for the monolayer case, i = 1, 2 correspond to the first and second conduction bands.

## ASSOCIATED CONTENT

### Supporting Information

Supporting Information: Figures S1-S27.

## AUTHOR INFORMATION

### Corresponding Authors

**Shoujun Zheng -** Centre for Quantum Physics, Key Laboratory of Advanced Optoelectronic Quantum Architecture and Measurement

(MOE), School of Physics, Beijing Institute of Technology, Beijing, 100081, China; Email: szheng@bit.edu.cn

**Wei Jiang -** Centre for Quantum Physics, Key Laboratory of Advanced Optoelectronic Quantum Architecture and Measurement (MOE), School of Physics, Beijing Institute of Technology, Beijing, 100081, China; Email: wjiang@bit.edu.cn

**Yan Xiong -** Analysis&Testing center, Beijing Institute of technology, Beijing, 100081, China; Email: xiongyan@bit.edu.cn

**Zhiwei Wang -** Centre for Quantum Physics, Key Laboratory of Advanced Optoelectronic Quantum Architecture and Measurement (MOE), School of Physics, Beijing Institute of Technology, Beijing, 100081, China; Email: zhiweiwang@bit.edu.cn

**Authors**

**Dan Guo -** Centre for Quantum Physics, Key Laboratory of Advanced Optoelectronic Quantum Architecture and Measurement (MOE), School of Physics, Beijing Institute of Technology, Beijing 100081, China

**Huiwen Wang -** Centre for Quantum Physics, Key Laboratory of Advanced Optoelectronic Quantum Architecture and Measurement (MOE), School of Physics, Beijing Institute of Technology, Beijing 100081, China

**Liu Yang -** Centre for Quantum Physics, Key Laboratory of Advanced

Optoelectronic Quantum Architecture and Measurement (MOE), School of Physics, Beijing Institute of Technology, Beijing 100081, China

**Weikang Dong -** Centre for Quantum Physics, Key Laboratory of Advanced Optoelectronic Quantum Architecture and Measurement (MOE), School of Physics, Beijing Institute of Technology, Beijing 100081, China

**Boyu Xu -** Centre for Quantum Physics, Key Laboratory of Advanced Optoelectronic Quantum Architecture and Measurement (MOE), School of Physics, Beijing Institute of Technology, Beijing 100081, China

**Shuang Du -** Centre for Quantum Physics, Key Laboratory of Advanced Optoelectronic Quantum Architecture and Measurement (MOE), School of Physics, Beijing Institute of Technology, Beijing 100081, China

**Xuyan Rui -** Centre for Quantum Physics, Key Laboratory of Advanced Optoelectronic Quantum Architecture and Measurement (MOE), School of Physics, Beijing Institute of Technology, Beijing 100081, China

**Qingrong Liang -** Centre for Quantum Physics, Key Laboratory of Advanced Optoelectronic Quantum Architecture and Measurement (MOE), School of Physics, Beijing Institute of Technology, Beijing 100081, China

**Kenji Watanabe -** National Institute for Materials Science, 1-1 Namiki, Tsukuba 303-0044, Japan

**Takashi Taniguchi -** National Institute for Materials Science, 1-1 Namiki, Tsukuba 303-0044, Japan

**Jiadong Zhou -** Centre for Quantum Physics, Key Laboratory of Advanced Optoelectronic Quantum Architecture and Measurement (MOE), School of Physics, Beijing Institute of Technology, Beijing 100081, China

## Author Contributions

D.G. fabricated all the devices and obtained the data. H.W. and W.J. performed the first-principles calculation and theoretical analysis. L.Y. and Z.W. synthesized the $ReSe_2$ sample *via* chemical vapor transport method. W.D. finished the TEM measurements. B.X., S.D., X.R. and Q.L. assisted the device fabrications and optical and electronic tests. K.W. and T.T. synthesized *h*-BN samples. S.Z. and J.Z. supervised the project. All authors participated in scientific discussion and contributed on the manuscript.

## Notes

The authors declare no competing financial interest.

## ACKNOWLEDGMENTS

This work was supported by Natural Science Foundation of China grants (No.12104050 and No. 62375018), National Key Research and

Development Program of China (No. 2022YFA1203900) and Beijing Institute of Technology Research Fund Program for Young Scholars.

## REFERENCES


(1) Mishchenko, A.; Tu, J. S.; Cao, Y.; Gorbachev, R. V.; Wallbank, J. R.; Greenaway, M. T.; Morozov, V. E.; Morozov, S. V.; Zhu, M. J.; Wong, S. L.; Withers, F.; Woods, C. R.; Kim, Y. J.; Watanabe, K.; Taniguchi, T.; Vdovin, E. E.; Makarovsky, O.; Fromhold, T. M.; Fal'ko, V. I.; Geim, A. K., et al. Twist-Controlled Resonant Tunnelling in Graphene/Boron Nitride/Graphene Heterostructures. *Nat. Nanotechnol.* **2014,** 9, 808-813.

(2) Asada, M.; Suzuki, S.;Kishimoto, N. Resonant Tunneling Diodes for Sub-Terahertz and Terahertz Oscillators. *Jpn. J. of Appl. Phys.* **2008,** 47, 4375.

(3) Sun, M.; Fang, Q.; Xie, D.; Sun, Y.; Xu, J.; Teng, C.; Dai, R.; Yang, P.; Li, Z.; Li, W.;Zhang, Y. Novel Transfer Behaviors in 2D $MoS_2$/$WSe_2$ Heterotransistor and Its Applications in Visible-Near Infrared Photodetection. *Adv. Electron. Mater.* **2017,** 3, 1600502.

(4) Qiu, C.; Liu, F.; Xu, L.; Deng, B.; Xiao, M.; Si, J.; Lin, L.; Zhang, Z.; Wang, J.; Guo, H.; Peng, H.;Peng, L.-M. Dirac-Source Field-Effect Transistors as Energy-Efficient, High-Performance Electronic Switches. *Science (New York, N.Y.)* **2018,** 361, 387-392.

(5) Ma, Z.; Zhang, Q.; Tao, L.; Wang, Y.; Sando, D.; Zhou, J.; Guo, Y.; Lord, M.; Zhou, P.; Ruan, Y.; Wang, Z.; Hamilton, A.; Gruverman, A.; Tsymbal, E. Y.; Zhang, T.;Valanoor, N. A Room-Temperature Ferroelectric Resonant Tunneling Diode. *Adv. Mater.* **2022,** 34, 2205359.

(6) Broekaert, T. P. E.; Brar, B.; Wagt, J. P. A. v. d.; Seabaugh, A. C.; Morris, F. J.; Moise, T. S.; Beam, E. A.;Frazier, G. A. A Monolithic 4-Bit 2-Gsps Resonant Tunneling Analog-to-Digital Converter. *IEEE J. Solid-State Circuits* **1998,** 33, 1342-1349.

(7) Cao, H.; Klimovitch, G.; Björk, G.;Yamamoto, Y. Direct Creation of Quantum Well Excitons by Electron Resonant Tunneling. *Phys. Rev. Lett.* **1995,** 75, 1146-1149.

(8) Sun, J. P.; Haddad, G. I.; Mazumder, P.;Schulman, J. N. Resonant Tunneling Diodes: Models and Properties. *Proc. IEEE* **1998,** 86, 641-660.

(9) Wang, L.; Papadopoulos, S.; Iyikanat, F.; Zhang, J.; Huang, J.; Taniguchi, T.; Watanabe, K.; Calame, M.; Perrin, M. L.; García de Abajo, F. J.;Novotny, L. Exciton-Assisted Electron Tunnelling in van der Waals Heterostructures. *Nat. Mater.* **2023,** 22, 1094-1099.

(10) Xu, K.; Wynne, E.;Zhu, W. Resonant Tunneling and Negative Differential Resistance in Black Phosphorus Vertical Heterostructures. *Adv. Electron. Mater.* **2020,** 6, 2000318.

(11) Shi, J.; Liu, M.; Wen, J.; Ren, X.; Zhou, X.; Ji, Q.; Ma, D.; Zhang, Y.; Jin, C.; Chen, H.; Deng, S.; Xu, N.; Liu, Z.;Zhang, Y. All Chemical Vapor Deposition Synthesis and Intrinsic Bandgap Observation of $MoS_2$/Graphene Heterostructures. *Adv. Mater.* **2015,** 27, 7086-7092.

(12) Nguyen, L.-N.; Lan, Y.-W.; Chen, J.-H.; Chang, T.-R.; Zhong, Y.-L.; Jeng, H.-T.; Li, L.-J.;Chen, C.-D. Resonant Tunneling through Discrete Quantum States in Stacked Atomic-Layered $MoS_2$. *Nano Lett.* **2014,** 14, 2381-2386.

(13) Campbell, P. M.; Tarasov, A.; Joiner, C. A.; Ready, W. J.;Vogel, E. M. Enhanced Resonant Tunneling in Symmetric 2D Semiconductor Vertical Heterostructure Transistors. *ACS Nano* **2015,** 9, 5000-5008.

(14) Kim, K.; Prasad, N.; Movva, H. C. P.; Burg, G. W.; Wang, Y.; Larentis, S.; Taniguchi, T.; Watanabe, K.; Register, L. F.;Tutuc, E. J. N. l. Spin-Conserving Resonant Tunneling in Twist-Controlled $WSe_2$-hBN-$WSe_2$ Heterostructures. *Nano Lett.* **2018,** 18, 5967-5973.

(15) Britnell, L.; Gorbachev, R. V.; Geim, A. K.; Ponomarenko, L. A.; Mishchenko, A.; Greenaway, M. T.; Fromhold, T. M.; Novoselov, K. S.;Eaves, L. Resonant Tunnelling and Negative Differential

Conductance in Graphene Transistors. *Nat. Commun.* **2013,** 4, 1794.
(16) Srivastava, P. K.; Hassan, Y.; de Sousa, D. J. P.; Gebredingle, Y.; Joe, M.; Ali, F.; Zheng, Y.; Yoo, W. J.; Ghosh, S.; Teherani, J. T.; Singh, B.; Low, T.;Lee, C. Resonant Tunnelling Diodes Based on Twisted Black Phosphorus Homostructures. *Nat. Electron.* **2021,** 4, 269-276.
(17) Xiong, X.; Huang, M.; Hu, B.; Li, X.; Liu, F.; Li, S.; Tian, M.; Li, T.; Song, J.;Wu, Y. A Transverse Tunnelling Field-Effect Transistor Made From a van der Waals Heterostructure. *Nat. Electron.* **2020,** 3, 106-112.
(18) Cao, Y.; Fatemi, V.; Fang, S.; Watanabe, K.; Taniguchi, T.; Kaxiras, E.;Jarillo-Herrero, P. Unconventional Superconductivity in Magic-Angle Graphene Superlattices. *Nature* **2018,** 556, 43-50.
(19) Song, T.; Cai, X.; Tu, M. W.-Y.; Zhang, X.; Huang, B.; Wilson, N. P.; Seyler, K. L.; Zhu, L.; Taniguchi, T.; Watanabe, K.; McGuire, M. A.; Cobden, D. H.; Xiao, D.; Yao, W.;Xu, X. Giant Tunneling Magnetoresistance in Spin-Filter van der Waals Heterostructures. *Science (New York, N.Y.)* **2018,** 360, 1214-1218.
(20) Zheng, Z.; Ma, Q.; Bi, Z.; de la Barrera, S.; Liu, M.-H.; Mao, N.; Zhang, Y.; Kiper, N.; Watanabe, K.; Taniguchi, T.; Kong, J.; Tisdale, W. A.; Ashoori, R.; Gedik, N.; Fu, L.; Xu, S.-Y.;Jarillo-Herrero, P. Unconventional Ferroelectricity in Moiré Heterostructures. *Nature* **2020,** 588, 71-76.
(21) Dai, Y.; Qi, P.; Tao, G.; Yao, G.; Shi, B.; Liu, Z.; Liu, Z.; He, X.; Peng, P.; Dang, Z.; Zheng, L.; Zhang, T.; Gong, Y.; Guan, Y.; Liu, K.;Fang, Z. Phonon-Assisted Upconversion in Twisted Two-Dimensional Semiconductors. *Light Sci. Appl.* **2023,** 12, 6.
(22) Fallahazad, B.; Lee, K.; Kang, S.; Xue, J.; Larentis, S.; Corbet, C.; Kim, K.; Movva, H. C. P.; Taniguchi, T.; Watanabe, K.; Register, L. F.; Banerjee, S. K.;Tutuc, E. Gate-Tunable Resonant Tunneling in Double Bilayer Graphene Heterostructures. *Nano Lett.* **2015,** 15, 428-433.
(23) Hu, G.; Ou, Q.; Si, G.; Wu, Y.; Wu, J.; Dai, Z.; Krasnok, A.; Mazor, Y.; Zhang, Q.; Bao, Q.; Qiu, C.-W.;Alù, A. Topological Polaritons and Photonic Magic Angles in Twisted $\alpha$-$MoO_3$ Bilayers. *Nature* **2020,** 582, 209-213.
(24) Liao, M.; Wei, Z.; Du, L.; Wang, Q.; Tang, J.; Yu, H.; Wu, F.; Zhao, J.; Xu, X.; Han, B.; Liu, K.; Gao, P.; Polcar, T.; Sun, Z.; Shi, D.; Yang, R.;Zhang, G. Precise Control of the Interlayer Twist Angle in Large Scale $MoS_2$ Homostructures. *Nat. Commun.* **2020,** 11, 2153.
(25) Sun, T.; Chen, R.; Ma, W.; Wang, H.; Yan, Q.; Luo, J.; Zhao, S.; Zhang, X.;Li, P. Van der Waals Quaternary Oxides for Tunable Low-Loss Anisotropic Polaritonics. *Nat. Nanotechnol.* **2024,** 19, 758-765.
(26) Sun, X.; Suriyage, M.; Khan, A. R.; Gao, M.; Zhao, J.; Liu, B.; Hasan, M. M.; Rahman, S.; Chen, R.-s.; Lam, P. K.;Lu, Y. Twisted van der Waals Quantum Materials: Fundamentals, Tunability, and Applications. *Chem. Rev.* **2024,** 124, 1992-2079.
(27) Zheng, S.; Jo, S.; Kang, K.; Sun, L.; Zhao, M.; Watanabe, K.; Taniguchi, T.; Moon, P.; Myoung, N.;Yang, H. Resonant Tunneling Spectroscopy to Probe the Giant Stark Effect in Atomically Thin Materials. *Adv. Mater.* **2020,** 32, 1906942.
(28) Ghazaryan, D. A.; Misra, A.; Vdovin, E. E.; Watanabe, K.; Taniguchi, T.; Morozov, S. V.; Mishchenko, A.;Novoselov, K. S. Twisted Monolayer and Bilayer Graphene for Vertical Tunneling Transistors. *Appl. Phys. Lett.* **2021,** 118, 183106.
(29) Kuzmina, A.; Parzefall, M.; Back, P.; Taniguchi, T.; Watanabe, K.; Jain, A.;Novotny, L. Resonant Light Emission from Graphene/Hexagonal Boron Nitride/Graphene Tunnel Junctions. *Nano Lett.* **2021,** 21, 8332-8339.

(30) Jang, J.; Yoo, H. M.; Pfeiffer, L. N.; West, K. W.; Baldwin, K. W.;Ashoori, R. C. Full Momentum- and Energy-Resolved Spectral Function of a 2D Electronic System. *Science (New York, N.Y.)* **2017,** 358, 901-906.
(31) Keren, I.; Dvir, T.; Zalic, A.; Iluz, A.; LeBoeuf, D.; Watanabe, K.; Taniguchi, T.;Steinberg, H. Quantum-Dot Assisted Spectroscopy of Degeneracy-Lifted Landau Levels in Graphene. *Nat. Commun.* **2020,** 11, 3408.
(32) Kim, E.; Hwang, G.; Kim, D.; Won, D.; Joo, Y.; Zheng, S.; Watanabe, K.; Taniguchi, T.; Moon, P.; Kim, D.-W.; Sun, L.;Yang, H. Orbital Gating Driven by Giant Stark Effect in Tunneling Phototransistors. *Adv. Mater.* **2022,** 34, 2106625.
(33) Takeyama, K.; Moriya, R.; Okazaki, S.; Zhang, Y.; Masubuchi, S.; Watanabe, K.; Taniguchi, T.; Sasagawa, T.;Machida, T. Resonant Tunneling Due to van der Waals Quantum-Well States of Few-Layer $WSe_2$ in $WSe_2$/h-BN/$p^+$-$MoS_2$ Junction. *Nano Lett.* **2021,** 21, 3929-3934.
(34) Greenaway, M. T.; Vdovin, E. E.; Mishchenko, A.; Makarovsky, O.; Patanè, A.; Wallbank, J. R.; Cao, Y.; Kretinin, A. V.; Zhu, M. J.; Morozov, S. V.; Fal'ko, V. I.; Novoselov, K. S.; Geim, A. K.; Fromhold, T. M.;Eaves, L. Resonant Tunnelling Between the Chiral Landau States of Twisted Graphene Lattices. *Nat. Phys.* **2015,** 11, 1057-1062.
(35) Wallbank, J. R.; Ghazaryan, D.; Misra, A.; Cao, Y.; Tu, J. S.; Piot, B. A.; Potemski, M.; Pezzini, S.; Wiedmann, S.; Zeitler, U.; Lane, T. L. M.; Morozov, S. V.; Greenaway, M. T.; Eaves, L.; Geim, A. K.; Fal'ko, V. I.; Novoselov, K. S.;Mishchenko, A. Tuning the Valley and Chiral Quantum State of Dirac Electrons in van der Waals Heterostructures. *Science (New York, N.Y.)* **2016,** 353, 575-579.
(36) Shim, J.; Oh, S.; Kang, D.-H.; Jo, S.-H.; Ali, M. H.; Choi, W.-Y.; Heo, K.; Jeon, J.; Lee, S.; Kim, M.; Song, Y. J.;Park, J.-H. Phosphorene/Rhenium Disulfide Heterojunction-Based Negative Differential Resistance Device for Multi-Valued Logic. *Nat. Commun.* **2016,** 7, 13413.
(37) Shim, J.; Jo, S.-H.; Kim, M.; Song, Y. J.; Kim, J.;Park, J.-H. Light-Triggered Ternary Device and Inverter Based on Heterojunction of van der Waals Materials. *ACS Nano* **2017,** 11, 6319-6327.
(38) Blöchl, P. E. Projector Augmented-Wave Method. *Phys. Rev. B* **1994,** 50, 17953-17979.
(39) Perdew, J. P.; Burke, K.;Ernzerhof, M. Generalized Gradient Approximation Made Simple. *Phys. Rev. Lett.* **1996,** 77, 3865-3868.
(40) Kresse, G.;Hafner, J. Ab Initio Molecular Dynamics for Liquid Metals. *Phys. Rev. B* **1993,** 47, 558-561.

# ToC image

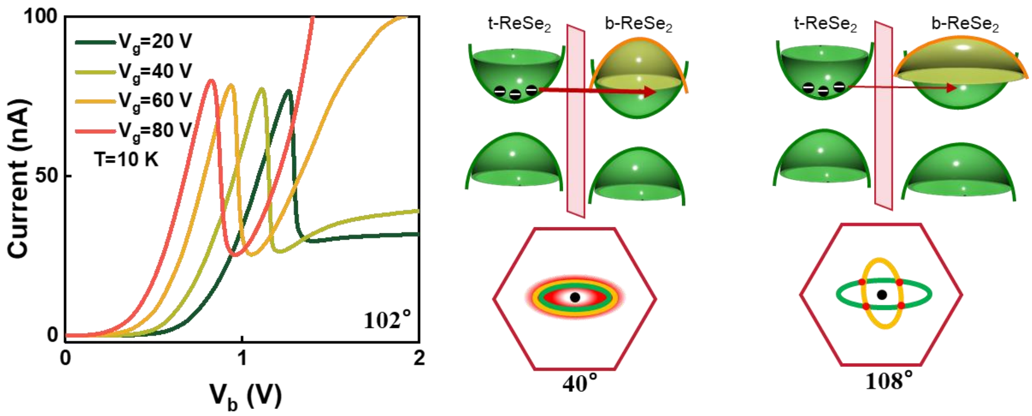


ToC caption: An anisotropic resonant tunneling transistor based on anisotropic $ReSe_2$ is reported, where peak-to-valley ratio exhibits a strong dependence on the twist angle between the two $ReSe_2$ layers, reaching a maximum at the twist angle of 102° due to the modulation of the joint density of states and suppression of the valley current.